JOURNAL OF COMPUTATIONAL PHYSICS 106, 42–51 (1993)

A Chebyshev Spectral Collocation Method for the Solution of the Reynolds Equation of Lubrication

PETER E. RAAD

Mechanical Engineering Department, Southern Methodist University, Dallas, Texas 75275

AND

ANDREAS KARAGEORGHIS*

Department of Mathematics and Statistics, University of Cyprus, P.O. Box 537, Nicosia, Cyprus

Received July 22, 1991; revised September 9, 1992

A multi-domain, Chebyshev collocation method is presented for the solution of ultra-thin gas bearing problems. The behavior of the flow varies across the computational domain with very sharp gradients occurring in the side and trailing edge boundary layers. The decomposition of the computational domain allows independent control over the representation of the solution in each subdomain. A multi-parameter continuation scheme is used to facilitate the convergence as the parameters of the problem are varied over a wide range. The method is shown to be well suited for the simulation of lubrication flow between textured surfaces even in the presence of very steep pressure boundary layers.

1. INTRODUCTION

Hydrodynamic lubrication has received much attention since it was discovered in the late 19th century that a thin layer of fluid separating two surfaces in relative motion facilitates that motion. Such thin fluid films are referred to as fluid bearings. When the relative motion itself brings about a force large enough to provide the necessary separation, a self-acting bearing is said to have developed. Self-acting bearings find widespread use, especially in high-speed, low-friction, precision instruments, such as magnetic disk drives. The disk drive relies on an air bearing to help support the read/write head a fraction of a micrometer away from a magnetic disk spinning at thousands of revolutions per minute. The head carries the magnetic transducer that is used to read from and write to the disk. When the drive is started, the disk begins to spin with the head dragging along its surface. The rubbing action between the two surfaces generates large friction forces that subject the two surfaces to wear. Since these forces are proportional to the relative velocity between the disk and the head, early head lift-off is highly desirable. In order to help the surfaces resist stiction and separate at the lowest possible velocities, disks are artificially textured during manufacturing with circumferential grooves of characteristic dimensions in the submicrometer range.

Due to viscous entrainment, air is pulled through betwen the surfaces of the head and the disk and is compressed in the wedge-shaped clearance, giving rise to an air bearing. Bearing pressure and flow rate increase as the spinning velocity of the disk increases. When the normal force generated by the air bearing exceeds the weight of the head and the force applied by the flexure arm from which the read/write head is suspended, the head takes off and begins to fly over the disk surface. The nominal clearance between the head and the disk, called the "flying height," is around 0.1 μm in current magnetic drives. The continued thrust toward smaller drives and larger bit recording densities continues at a very rapid pace. The accurate simulation of the air bearing plays an essential role in the design of new head shapes that will allow higher recording capacities through reductions in flying heights. The simulation of an air bearing interface is accomplished by the solution of the Reynolds equation of lubrication and requires the bulk of the computational effort involved in the design process. The inclusion of surface roughness effects greatly intensifies the computational effort, but it is becoming unavoidable since the nominal flying heights and the surface texture amplitudes are now of the same order of magnitude.

In the past decade, several researchers have investigated the effects of surface roughness on the head/disk air bearing interface. The majority of the simulations have used finite difference and some finite element methods. Both methods

* Parts of this work were performed while this author was in the mathematics department at Southern Methodist University, Dallas, Texas 75275.

0021-9991/93 $5.00

have proved satisfactory thus far, especially when most designs have ignored the effects of surface roughness. An example of a finite element solution of an air bearing problem is that of Mitsuya [6] in which he investigated the effects of molecular slip flow on smooth air bearings. White and Nigam [14] presented a factored-implicit, finite difference method for the solution of the Reynolds equation for thin air bearings. White *et al.* [16] used the same method to study the effects of stationary surface roughness on an infinitely wide, wedge gas bearing. Raad and White [10] added a taper to the slider and showed that surface roughness effects are local in nature, making the results applicable to a wide range of bearing configurations. Raad and Kuria [9] extended the analysis to include roughness patterns on both the stationary and translating surfaces. Varghese and Raad [13] used a second-order accurate finite difference method to solve the transient Reynolds equation for three-dimensional roughness configurations on both the stationary and translating surfaces. They found that, in general, a minimum of 20, and as many as 120, grid points per roughness wave were necessary to accurately resolve the spatial and temporal variations in the air pressure. Some of the flow parameters that were studied accentuated the degree of nonlinearity of the problem, making it necessary to employ the higher number of grid points per texture wave. The large grid point per wave requirement by finite difference methods motivates the need to investigate higher order methods. Recently, spectral methods have been gaining popularity and have proven effective for the solution of problems in computational fluid dynamics [3].

This study presents an investigation of the use of Chebyshev spectral collocation methods to accurately solve the Reynolds equation with a significant reduction in the required number of degrees of freedom per texture wave. At high fluid velocities and low flow clearances, pressure boundary layers develop near the side and trailing edges of the bearing. The dramatically different flow behavior in the different regions of the computational domain demands the use of an efficient domain decomposition strategy. In this work, a four-subdomain decomposition scheme is employed with three of the subdomains used to describe the boundary layers.

2. DESCRIPTION OF THE PROBLEM

Fluid flow between closely separated, nearly parallel surfaces in relative motion is governed by the Reynolds equation of hydrodynamic lubrication which is derived from the Navier–Stokes equations by making the usual lubrication assumptions of negligible inertia and gravity effects. Given the ultra-thin spacing of bearings, the pressure gradient in the perpendicular direction between the two surfaces vanishes. The resulting Reynolds equation of lubrication represents a balance between viscous and pressure diffusion effects in two dimensions. Considering an isothermal state, the flow of a gas bearing between a stationary slider and a translating surface is governed by

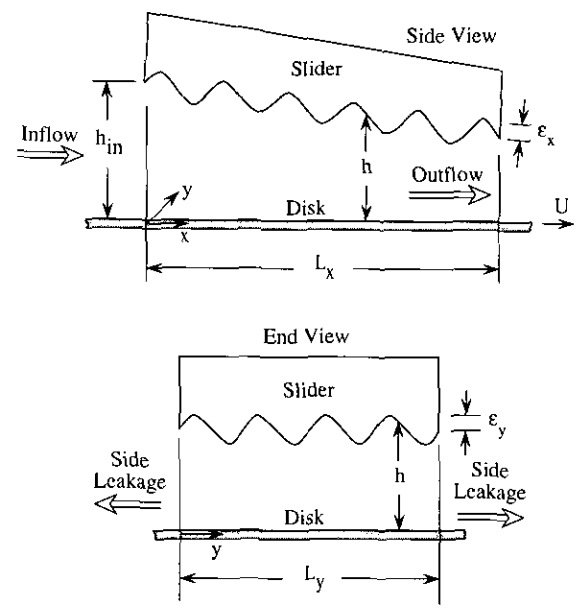

FIG. 1. Geometry of air bearing between stationary rough slider and translating smooth disk.

$$\frac{\partial}{\partial x}\left(h^3 P \frac{\partial P}{\partial x}\right) + R^2 \frac{\partial}{\partial y}\left(h^3 P \frac{\partial P}{\partial y}\right) = \Lambda \frac{\partial}{\partial x}(Ph). \quad (2.1)$$

The above Reynolds equation is applicable to flow between two surfaces in relative motion even when the surfaces are rough. However, when the local rate of change in the roughness becomes very large, the assumption of a negligible pressure gradient across the film thickness no longer applies and the Reynolds equation breaks down. This type of roughness is referred to as Stokes roughness and requires the solution of the Navier–Stokes equations instead of the Reynolds equation. In this work, the roughness used is sinusoidal in nature and is representative of the artificial texture fabricated into the disks during manufacturing in order to help the moving surfaces resist stiction.

The clearance height of the slider geometry shown in Fig. 1 is given by

$$h(x, y) = h_{in} + (1 - h_{in})x + \varepsilon_x \sin(\beta_x x) + \varepsilon_y \sin(\beta_y y + \phi). \quad (2.2)$$

All the variables are non-dimensional and are defined as follows:

*	Superscript indicating a corresponding dimensional variable.
h	Dimensionless bearing spacing, $h(x, y) = h^*(x, y)/h_0^*$.

h_0^* Mean trailing edge clearance, m.
h_{in} Dimensionless inlet bearing spacing, $h_{in} = h^*(0, y)/h_0^*$.
L_x^* Slider length, m.
L_y^* Slider width, m.
NWX Number of waves in the x-direction.
NWY Number of waves in the y-direction.
P Dimensionless fluid film pressure, $P(x, y) = P^*(x, y)/P_a^*$.
P_a^* Ambient pressure, Pa.
R Aspect ratio, $= L_x^*/L_y^*$.
U^* Axial relative velocity, m/s.
W Dimensionless load per unit width, $= \int_0^1 \int_0^1 (P-1)\, dx\, dy$.
x Dimensionless axial space coordinate, $= x^*/L_x^*$.
y Dimensionless transverse space coordinate, $= y^*/L_y^*$.
β_x Angular frequency of the stationary roughness in the x-direction, $= 2\pi\, NWX$.
β_y Angular frequency of the stationary roughness in the y-direction, $= 2\pi\, NWY$.
ε_x Dimensionless roughness amplitude in the x-direction, $= \varepsilon_x^*/h_0^*$.
ε_y Dimensionless roughness amplitude in the y-direction, $= \varepsilon_y^*/h_0^*$.
ϕ Phase angle for y-directional waves, radians.
Λ Dimensionless gas bearing number, $= (6\mu^* U^* L_x^*)/(P_a^* h_0^* h_0^*)$.
μ^* Dynamic viscosity, N-s/m^2.

3. THE NUMERICAL METHOD

Only half the computational domain is considered due to symmetry about the $y = 0.5$ line. This region is divided into four subdomains as shown in Fig. 2. In each subdomain the solution is approximated by $P^i(x, y)$, where

$$P^i(x, y) = \sum_{m=0}^{M_i} \sum_{n=0}^{N_i} a_{mn}^i T_m^i(x)\, \tilde{T}_n^i(y), \qquad i = \text{I, II, III, IV}. \tag{3.1}$$

The polynomials $T_m^i(x)$, $i = $ I, II, III, IV are the shifted Chebyshev polynomials on the intervals $[0, x_d]$, $[0, x_d]$, $[x_d, 1]$, $[x_d, 1]$, respectively. The polynomials $\tilde{T}_n^i(y)$, $i = $ I, II, III, IV are the shifted Chebyshev polynomials on the intervals $[y_d, 0.5]$, $[0, y_d]$, $[0, y_d]$, $[y_d, 0.5]$, respectively. To make the approximation conforming, that is, to force the pressure to be pointwise continuous at all the points on the subdomain interfaces, we need to take

$$M_{II} = M_I, \qquad M_{IV} = M_{III}, \qquad N_{III} = N_{II}, \qquad N_{IV} = N_I.$$

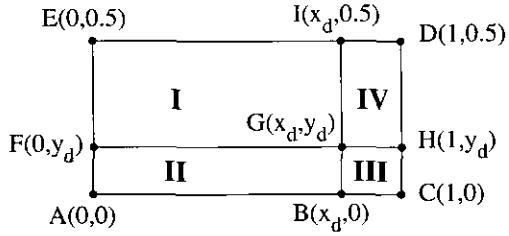

FIG. 2. Domain decomposition into four subregions.

The collocation points in each subregion in the x- and y-directions are taken to be the Gauss–Lobatto points [2]. In each region i ($i = $ I, II, III, IV), the differential equation is satisfied at the collocation points (x_K^i, y_L^i), $K = 1, ..., M_i - 1$; $L = 1, ..., N_i - 1$, where the points $\{x_K^i\}$, $K = 0, ..., M_i$, and $\{y_L^i\}$, $L = 0, ..., N_i$, are the Gauss–Lobatto points for subregion i in the x- and y-directions, respectively. The boundary condition on FE (region I) is collocated at all $N_I + 1$ collocation points, whereas the boundary condition on EI (region I) is collocated at M_I points (all the Gauss–Lobatto points except for the first one). In region II, the boundary condition on AF is imposed at N_{II} points (the first point is excluded). The boundary condition on BA is imposed at all $M_{II} + 1$ points. In region III, along CB, the boundary condition is imposed at all $M_{III} + 1$ collocation points, whereas along HC, the boundary condition is imposed at N_{III} points (excluding the first point). Finally in region IV, on DH the boundary condition is collocated at all $N_{IV} + 1$ points and the boundary condition on ID at M_{IV} points (excluding the first point). Because the boundary conditions are constants, the above choice of collocation points ensures that all boundary conditions are satisfied identically along the entire boundary.

On the interface between I and II the following continuity conditions are imposed:

$$P^{I}(x_K^{I}, y_d) = P^{II}(x_K^{II}, y_d), \qquad K = 1, ..., M_I, \tag{3.2}$$

$$\frac{\partial}{\partial y} P^{I}(x_K^{I}, y_d) = \frac{\partial}{\partial y} P^{II}(x_K^{II}, y_d), \qquad K = 1, ..., M_I - 1 \tag{3.3}$$

(recall that $M_I = M_{II}$).

Between II and III,

$$P^{II}(x_d, y_L^{II}) = P^{III}(x_d, y_L^{III}), \qquad L = 1, ..., N_{II}, \tag{3.4}$$

$$\frac{\partial}{\partial x} P^{II}(x_d, y_L^{II}) = \frac{\partial}{\partial x} P^{III}(x_d, y_L^{III}), \qquad L = 1, ..., N_{II} - 1 \tag{3.5}$$

(recall that $N_{II} = N_{III}$).

Between III and IV,

$$P^{III}(x_K^{III}, y_d) = P^{IV}(x_K^{IV}, y_d), \qquad K = 0, ..., M_{III} - 1, \tag{3.6}$$

$$\frac{\partial}{\partial y} P^{III}(x_K^{III}, y_d) = \frac{\partial}{\partial y} P^{IV}(x_K^{IV}, y_d), \qquad K = 1, ..., M_{III} - 1 \tag{3.7}$$

(recall that $M_{III} = M_{IV}$).

Between regions IV and I,

$$P^{\mathrm{I}}(x_d, y_L^{\mathrm{I}}) = P^{\mathrm{IV}}(x_d, y_L^{\mathrm{IV}}), \qquad L = 1, ..., N_{\mathrm{IV}} - 1, \tag{3.8}$$

$$\frac{\partial}{\partial x} P^{\mathrm{I}}(x_d, y_L^{\mathrm{I}}) = \frac{\partial}{\partial x} P^{\mathrm{IV}}(x_d, y_L^{\mathrm{IV}}), \qquad L = 1, ..., N_{\mathrm{IV}} - 1 \tag{3.9}$$

(recall that $N_{\mathrm{I}} = N_{\mathrm{IV}}$). Finally, the differential equation is satisfied at the point G of region IV.

The above choice of interface conditions ensures that the approximation to the pressure solution is continuous at all points across the element interfaces. The normal derivatives of the approximation are continuous at a finite number of points (i.e., the collocation points). For details concerning Poisson problems, see Karageorghis [5].

The total number of equations is equal to $M = (M_{\mathrm{I}} + 1)(N_{\mathrm{I}} + 1) + (M_{\mathrm{II}} + 1)(N_{\mathrm{II}} + 1) + (M_{\mathrm{III}} + 1)(N_{\mathrm{III}} + 1) + (M_{\mathrm{IV}} + 1)(N_{\mathrm{IV}} + 1)$ which is equal to the total number of unknown coefficients $\{a_{mn}^i\}$, $m = 0, ..., M_i$; $n = 0, ..., N_i$; and $i = \mathrm{I}, \mathrm{II}, \mathrm{III}$, and IV.

Solution of the Algebraic System. The discretization described in the previous section results in a mixed system of algebraic equations which needs to be solved for the unknown coefficients $\{a_{mn}^i\}$, $m = 0, ..., M_i$; $n = 0, ..., N_i$; and $i = \mathrm{I}, \mathrm{II}, \mathrm{III}$, and IV.

The system is solved using the NAG modification [7] of the hybrid Powell method [8] which is implemented in the NAG routines C05NBF and C05PBF. In the former, the user is not required to provide the Jacobian of the system (which is calculated internally), while in the latter the user is required to provide the Jacobian of the system, resulting in substantial savings in CPU time. In this study, the Jacobian was calculated exactly and provided to C05PBF.

For relatively small degrees of nonlinearity, both NAG solvers converged to the solution of the problem from the plane $P_i(x, y) = 1$, $i = \mathrm{I}, \mathrm{II}, \mathrm{III}, \mathrm{IV}$ (i.e., by initially taking $a_{00}^i = 1$, $a_{mn}^i = 0$, $m, n > 0$). For larger degrees of nonlinearity, however, convergence became gradually more difficult to achieve, and the use of a continuation scheme became necessary [12]. Initially, continuation in Λ was employed primarily. For large values of Λ, when more degrees of freedom were required to satisfactorily represent the solution, continuation in the coefficients a_{mn}^i was used as well (by adding more coefficients with zero values). When the thicknesses of the boundary layers decreased, x_d and y_d were changed accordingly through continuation. Finally, for cases involving two-dimensional texture and large values of the bearing number, continuation in the wave amplitudes, ε_x and ε_y, was performed as well. The implementation of this multi-parameter continuation scheme provided a mechanism for independent control of the problem parameters and resulted in substantial savings in the computational effort.

Once the coefficients $\{a_{mn}^i\}$ were evaluated, the pressure distribution was calculated from Eq. (3.1) at selected points in the computational domain. A useful physical quantity in the study of air bearing dynamics is the force generated by the air against the stationary and translating surfaces. This force, referred to as the load, was calculated from

$$W = 2 \int_0^{1/2} \int_0^1 (P(x, y) - 1)\, dx\, dy. \tag{3.10}$$

The factor of 2 is the result of symmetry about the $y = 0.5$ line. Clearly,

$$\begin{aligned} W = {} & 2 \int_{y_d}^{1/2} \int_0^{x_d} P^{\mathrm{I}}(x, y)\, dx\, dy \\ & + 2 \int_0^{y_d} \int_0^{x_d} P^{\mathrm{II}}(x, y)\, dx\, dy \\ & + 2 \int_0^{y_d} \int_{x_d}^1 P^{\mathrm{III}}(x, y)\, dx\, dy \\ & + 2 \int_{y_d}^{1/2} \int_{x_d}^1 P^{\mathrm{IV}}(x, y)\, dx\, dy - 1. \end{aligned} \tag{3.11}$$

The first integral yields

$$\begin{aligned} & 2 \int_{y_d}^{1/2} \int_0^{x_d} \sum_{m=0}^{M_{\mathrm{I}}} \sum_{n=0}^{N_{\mathrm{I}}} a_{mn}^{\mathrm{I}} T_m^{\mathrm{I}}(x)\, \tilde{T}_n^{\mathrm{I}}(y)\, dx\, dy \\ & \quad = 2 \sum_{m=0}^{M_{\mathrm{I}}} \sum_{n=0}^{N_{\mathrm{I}}} a_{mn}^{\mathrm{I}} \left(\int_0^{x_d} T_m^{\mathrm{I}}(x)\, dx \right) \\ & \qquad \times \left(\int_{y_d}^{1/2} \tilde{T}_n^{\mathrm{I}}(y)\, dy \right), \end{aligned} \tag{3.12}$$

where the definite integrals may be calculated exactly by the use of the properties of Chebyshev polynomials (see Fox and Parker [4]). For example,

$$\int_0^{x_d} T_0^{\mathrm{I}}(x)\, dx = \frac{x_d}{2} [T_1^{\mathrm{I}}(x_d) - T_1^{\mathrm{I}}(0)], \tag{3.13}$$

$$\int_0^{x_d} T_1^{\mathrm{I}}(x)\, dx = \frac{x_d}{8} [T_2^{\mathrm{I}}(x_d) - T_2^{\mathrm{I}}(0)], \tag{3.14}$$

$$\int_0^{x_d} T_m^{\mathrm{I}}(x)\, dx = \frac{x_d}{4} \left[\frac{T_{m+1}^{\mathrm{I}}(x_d) - T_{m+1}^{\mathrm{I}}(0)}{m+1} - \frac{T_{m-1}^{\mathrm{I}}(x_d) - T_{m-1}^{\mathrm{I}}(0)}{m-1} \right]. \tag{3.15}$$

4. NUMERICAL RESULTS

A total of three bearing geometries were investigated. In all cases, the ratio of inlet to trailing edge heights, h_{in}, was

2, and the bearing's aspect ratio, R, was 10. This choice of geometric parameters was motivated by current read/write head designs [1].

4.1. *Case* 1: *Smooth Bearing.* Fluid flows through the gap between the stationary and translating surfaces due to viscous entrainment. The fluid enters with a pressure equal to ambient and is compressed as it flows toward the side and trailing edges. Since the pressure on all sides is ambient, the pressure of the compressed fluid must return to ambient when the fluid exits either through the side or through the trailing edges. As a result, boundary layers are generated near those edges with thicknesses of orders $\Lambda^{-1/2}$ and Λ^{-1}, respectively [11, 13].

Figures 3a and b show combined surface and contour plots of the pressure distribution over the computational domain for $\Lambda = 2000$ and $\Lambda = 10^5$, respectively. The side and trailing edge boundary layers are evident for both cases, but are difficult to discern in the figures due to the closeness of the contour lines. An enlargement of a portion of the trailing edge boundary layer in Fig. 3a is shown in Fig. 3c, providing a better view of the pressure variations in that

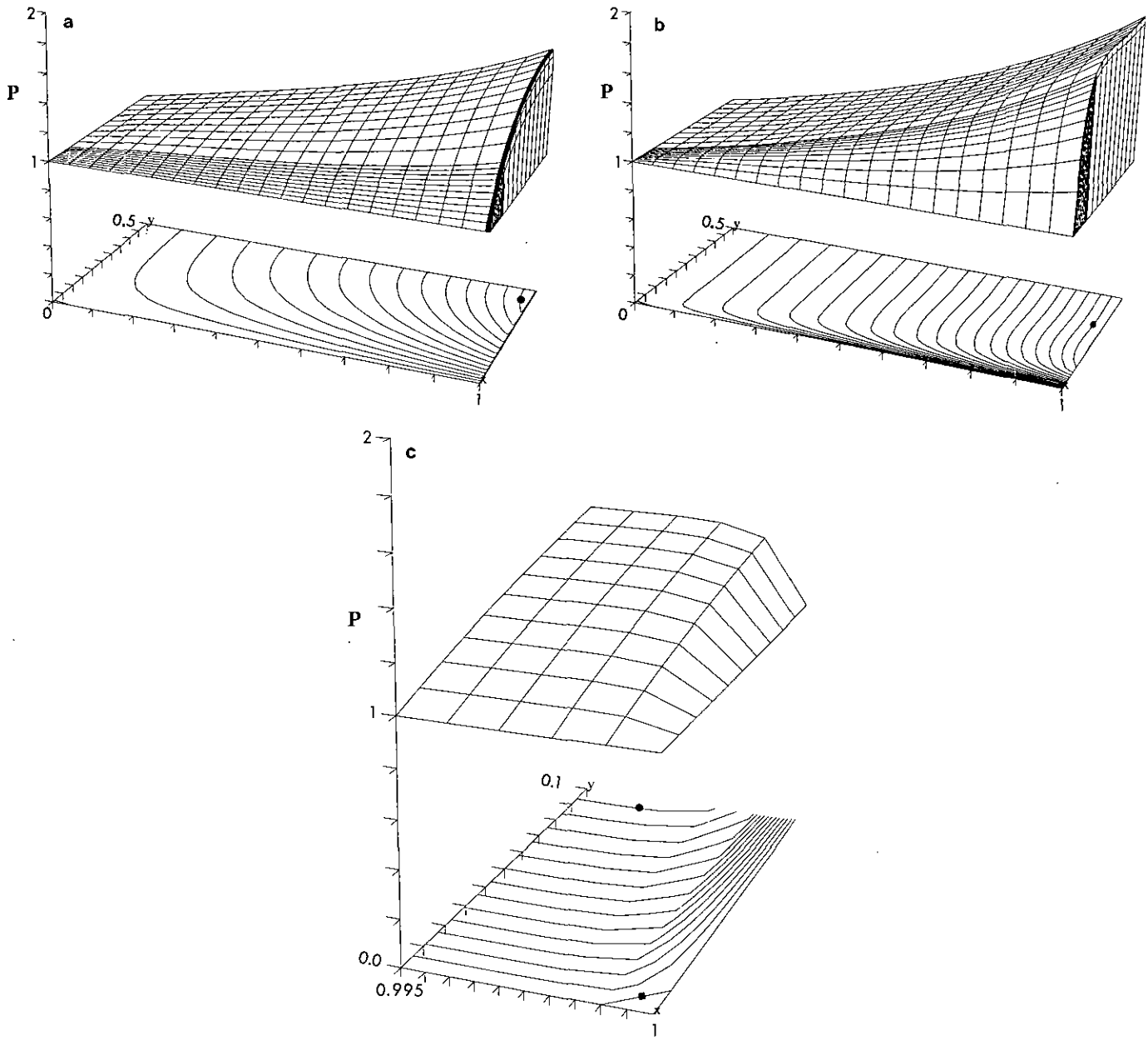

FIG. 3. (a) Pressure profile for a smooth bearing: $\Lambda = 2000$ ($P_{\min} = 1$, $P_{\max} = 1.7$, $\Delta P = 0.05$). (b) Pressure profile for a smooth bearing: $\Lambda = 10^5$ ($P_{\min} = 1$, $P_{\max} = 1.95$, $\Delta P = 0.05$). (c) Enlarged view of trailing edge boundary layer region in Fig. 3a ($P_{\min} = 1$, $P_{\max} = 1.325$, $\Delta P = 0.025$).

TABLE I

Convergence Results for a Smooth Bearing with $\Lambda = 2000$, $x_d = 0.99$, $y_d = 0.1$, and $N_I = N_{II} = N_{III} = N_{IV} = 4$

$M_I = M_{II}$	$M_{III} = M_{IV}$	W
14	14	0.219540
16	14	0.219754
18	14	0.219879
20	14	0.219950
20	16	0.219952
20	18	0.219953
20	20	0.219952

region. In these and all subsequent combined surface and contour plots, the figure caption includes the values of the minimum pressure contour, P_{min}, the maximum pressure contour, P_{max}, and the increment, ΔP. The ambient pressure contour, $P = 1$, always coincides with the $x = 0$ and $y = 0$ axes, but also may occur inside the computational domain. When it does, the $P = 1$ contour is identified by a rectangular symbol. The P_{max} contour is identified by a circular symbol while the contour of the smallest sub-ambient pressure, when present, is identified by triangular symbols.

As the bearing number, Λ, increases, the fluid velocity increases, and the side leakage decreases. Since more fluid is entrained toward the trailing edge, higher pressures are generated and, in turn, higher loads are obtained. Given the boundary layer thicknesses expected for the case of $\Lambda = 2000$, x_d and y_d were set equal to 0.99 and 0.1, respectively. The number of expansion coefficients was increased until the numerical results no longer changed,[1] and this was achieved for $M_I = M_{II} = 20$, $M_{III} = M_{IV} = 16$, and $N_I = N_{II} = N_{III} = N_{IV} = 4$. A summary of the continuation procedure used to achieve convergence for the preceding case is shown in Table I.

When Λ was increased to 10^5, the thickness of element III (or IV) had to be reduced to 5×10^{-4} while the resolution in the x-direction was increased to $M_I = M_{II} = 22$, and $M_{III} = M_{IV} = 38$. Since the pressure variations in the y-direction are relatively smooth, a small number of degrees of freedom is required even for large values of Λ. The use of four elements makes it possible to independently increase the number of degrees of freedom in the regions where sharp pressure gradients occur. The effect of increasing the gas bearing number (either by increasing the translating surface velocity or by decreasing the clearance height) on the load carrying capacity is shown in Fig. 4. As the bearing number approaches infinity, the load tends asymptotically to a

[1] To determine convergence the following criteria were examined: (a) the pressure profiles, both graphically and quantitatively; (b) the magnitudes of the coefficients; and (c) the generated bearing load.

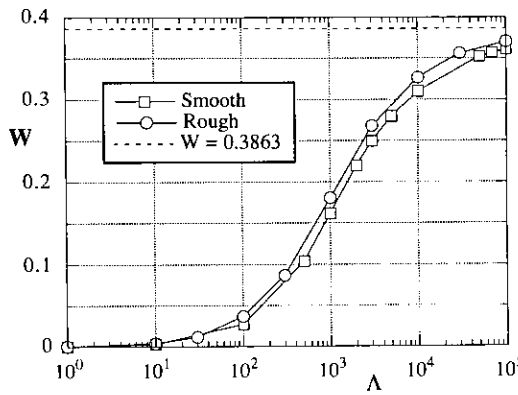

FIG. 4. Comparison of loads generated by a smooth slider and a slider with two-dimensional waviness ($NWX = 5$, $NWY = 4$, $\varepsilon_x = \varepsilon_y = 0.15$).

constant value, $W = 0.3863$. This phenomenon can be easily shown by analyzing the Reynolds equation for $\Lambda \to \infty$, which becomes

$$\frac{\partial}{\partial x}(P(x, y)\, h(x, y)) = 0 \tag{4.1}$$

$$\Rightarrow P(x, y)\, h(x, y) = C, \qquad \text{a constant.} \tag{4.2}$$

But $h(0, y) = h_{in}$ and $P(0, y) = 1$,

$$\Rightarrow P(x, y) = h_{in}/h(x, y). \tag{4.3}$$

Then,

$$W = \int_0^1 \int_0^1 [P(x, y) - 1]\, dx\, dy$$

$$= \int_0^1 \int_0^1 \left[\frac{h_{in}}{h(x, y)} - 1\right] dx\, dy \tag{4.4}$$

which is equal to 0.3863 for the given geometric parameters. Physically, as $\Lambda \to \infty$, the Couette effects represented by $\partial(Ph)/\partial x$ become dominant over the pressure diffusion terms on the left-hand side of the Reynolds equation (2.1). Of course, these pressure diffusion terms remain important

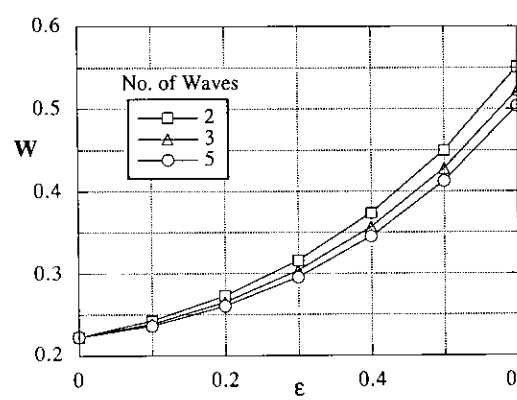

FIG. 5. Effect of wave amplitude and frequency on the bearing load.

inside the boundary layers and enable the pressure to return to ambient on the edges of the slider. Therefore, the solution to the limiting case, $\Lambda = \infty$, represents the "outer" solution and is useful in validating the numerical results as $\Lambda \to \infty$.

4.2. *Case 2: Stationary Texture in the x-Direction.* The motivation for considering texture comes from the fact that in current disk drives the nominal head flying heights are of the same order of magnitude as the average amplitude of the texture. Therefore, the effects of surface texture must be included in the simulation of self-acting, ultra-thin, air bearings.

In contrast to finite difference or finite element methods, spectral methods require fewer degrees of freedom to describe large spatial variations in the function [2, p. 259]. To demonstrate the effectiveness of the Chebyshev spectral collocation method, a small number of waves was prescribed on the stationary surface. Figure 5 shows the influence of the roughness amplitude and frequency on the bearing load for two, three, and five waves. Higher wave amplitudes give rise to larger pressure and clearance gradients with proportionally larger loads ensuing. These gradients which constitute the non-linear terms on the left-hand side of Eq. (2.1) are triggered by the presence of the surface texture and contribute to the rise in pressure. As shown in Figs. 6a–c, the increase in the wave amplitude

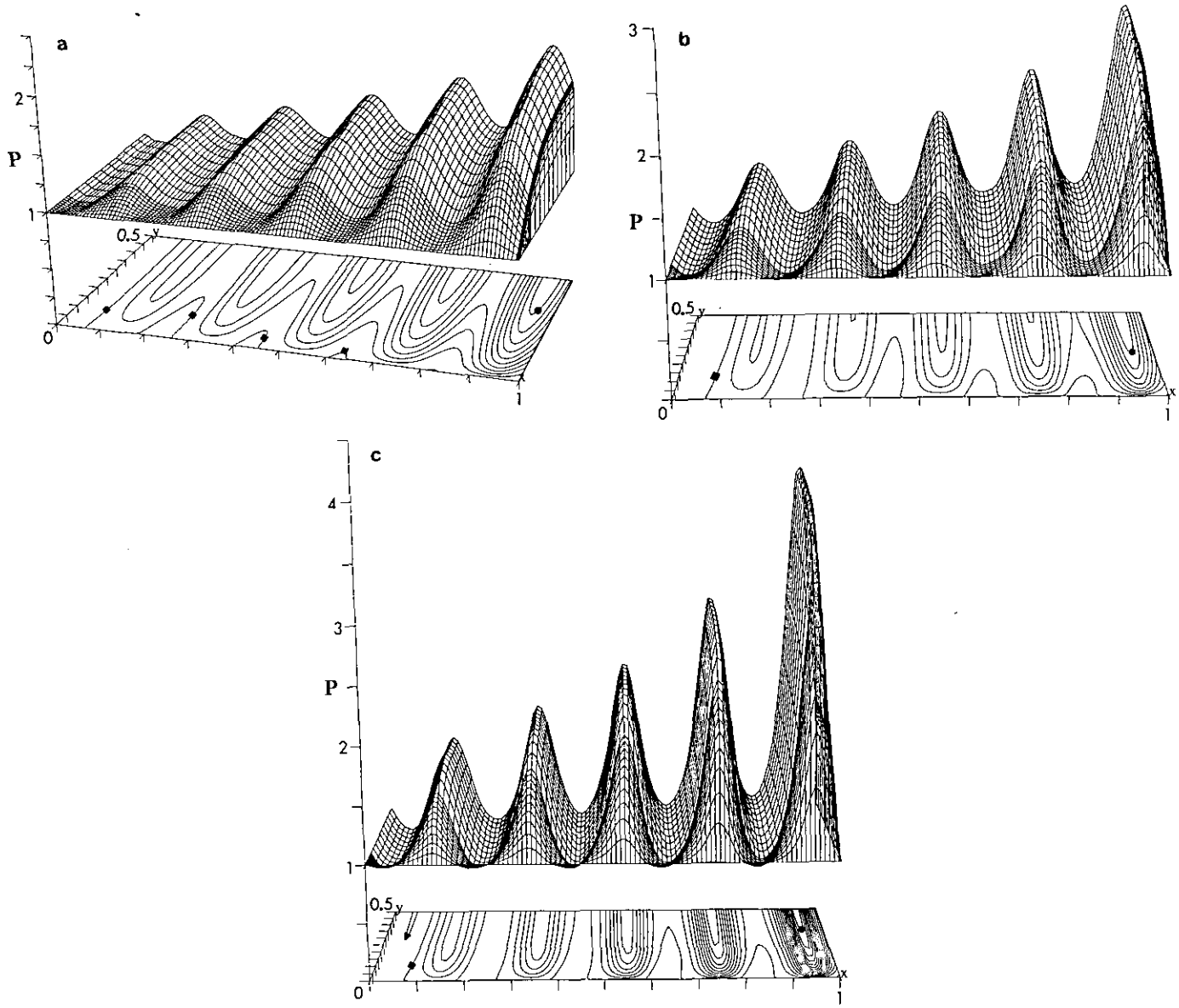

FIG. 6. (a) Pressure profile for a slider with five waves in the x-direction, and $\Lambda = 2000$: $\varepsilon_x = 0.2$ ($P_{\min} = 1$, $P_{\max} = 2$, $\Delta P = 0.1$). (b) Pressure profile for a slider with five waves in the x-direction, and $\Lambda = 2000$: $\varepsilon_x = 0.4$ ($P_{\min} = 1$, $P_{\max} = 2.6$, $\Delta P = 0.2$). (c) Pressure profile for a slider with five waves in the x-direction, and $\Lambda = 2000$: $\varepsilon_x = 0.6$ ($P_{\min} = 0.8$, $P_{\max} = 4$, $\Delta P = 0.2$).

(from 0.2 to 0.6) gives rise to larger pressure extrema, larger local pressure gradients, and steeper pressure boundary layers. The increase in the degree of non-linearity that results from larger amplitudes as well as the dramatic changes in the spatial gradients make it necessary to increase the number of degrees of freedom. In contrast, the frequency of the sinusoidal texture appears to have a slight effect on the load for the number of waves considered. The decrease in load with increasing frequency is slightly more significant at higher values of the wave amplitude even though the overall load behavior is qualitatively similar. For all three solutions, $x_d = 0.995$, $y_d = 0.1$, $M_{III} = M_{IV} = 14$, and $N_I = N_{II} = N_{III} = N_{IV} = 4$. For $\varepsilon = 0.2$, 0.4, and 0.6, $M_I = M_{II} = 31$, 35, and 49, respectively. Because the bearing number was fixed, the thicknesses of the boundary layers remained unchanged, requiring the same number of degrees of freedom in elements III and IV for all values of ε considered. A significant reduction in the number of degrees of freedom required per texture wave was observed in comparison to previously used finite difference methods [13]. In the latter work, a minimum of 20, and as many as 120, grid points per texture wave were necessary to resolve accurately the spatial variations in the air pressure. In addition, when Chebyshev spectral collocation was used without decomposition, a large number of collocation points was required to resolve the boundary layers on the edges of the domain, resulting in a finer-than-necessary resolution inside the computational domain.

A note of physical interest can be made with regard to sub-ambient pressures seen in Figs. 6a and b. Since the pressure varies as the inverse of the clearance height for large values of Λ (per Eq. (4.3)), an increase in the clearance height (such as the one that can be noted near $x = 0$) results in a decrease in the pressure. But, since the pressure at $x = 0$ is ambient, any decrease in the pressure will give rise to a region of sub-ambient pressures. Such a region may be observed also in Fig. 8 which will be discussed in the following section.

4.3. *Case* 3: *Stationary Surface Texture.* The last case considered involved stationary texture with five waves in the x-direction and four waves in the y-direction. The wave amplitude in each direction was set equal to 0.15, resulting in a total maximum blockage effect of 0.3. Figure 7 shows the clearance as well as the distribution of the Gauss–Lobatto collocation points used. As noted previously, computations were performed over half the bearing width due to symmetry about the $y = 0.5$ line. For the height function, $h(x, y)$, to be symmetric about $y = 0.5$, a 90° phase shift (ϕ) was included in the calculations (see Eq. (2.2)). The domain decomposition and spectral expansion parameters for this case are listed in Table II.

The pressure solutions for the three Λ values, 10^2, 10^3, 10^5, are plotted in Figs. 8a–c, respectively. Clearly, larger

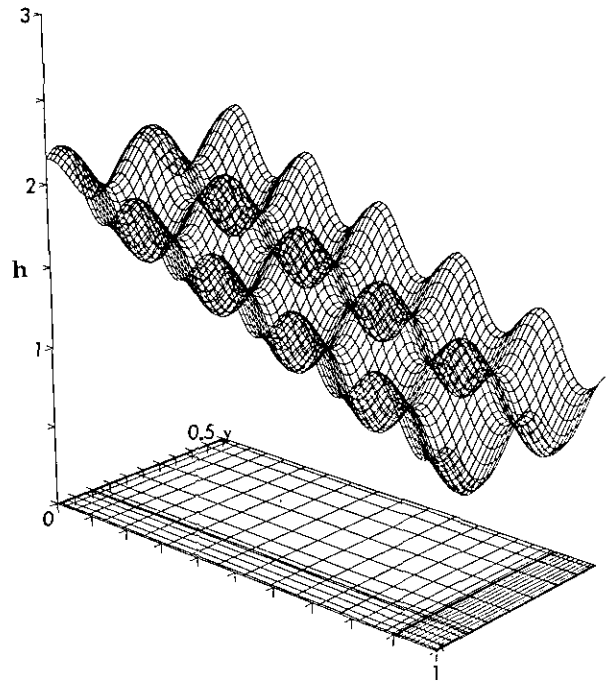

FIG. 7. Bearing clearance profile and four-subdomain, two-dimensional Gauss–Lobatto collocation grid ($NWX = 5$, $NWY = 4$, $\varepsilon_x = \varepsilon_y = 0.15$).

values of the bearing number result in significantly narrower trailing edge boundary layers. To allow a closer inspection of the pressure variations in the trailing edge region of Fig. 8b, an enlargement of a portion of that region is provided in Fig. 8d. The advantage of the multi-element formulation is confirmed upon examination of Table II, where it can be seen that much higher grid resolutions may be implemented in regions III and IV without directly affecting regions I and II. In the latter regions, approximately five collocation points per wave are required to accurately resolve the pressure spatial variations. The same observation can be made concerning the waviness in the y-direction. Since the thickness of the side boundary layer (near $x = 0$) is of $\mathbf{O}(\Lambda^{-1/2})$, a proportionally smaller number of collocation points is required to resolve the relatively smaller transverse (or y) pressure gradients. The shape of the clearance is manifested through the pressure field with the details becoming sharper as Λ increases. As previously discussed,

TABLE II

Variation of Geometric and Expansion Parameters for $\varepsilon_x = \varepsilon_y = 0.15$

Λ	y_d	x_d	$M_I = M_{II}$	$M_{III} = M_{IV}$	$N_I = N_{IV}$	$N_{II} = N_{III}$
10^2	0.1	0.99	20	18	8	6
10^3	0.1	0.995	20	22	8	6
10^5	0.1	0.9995	22	36	12	6

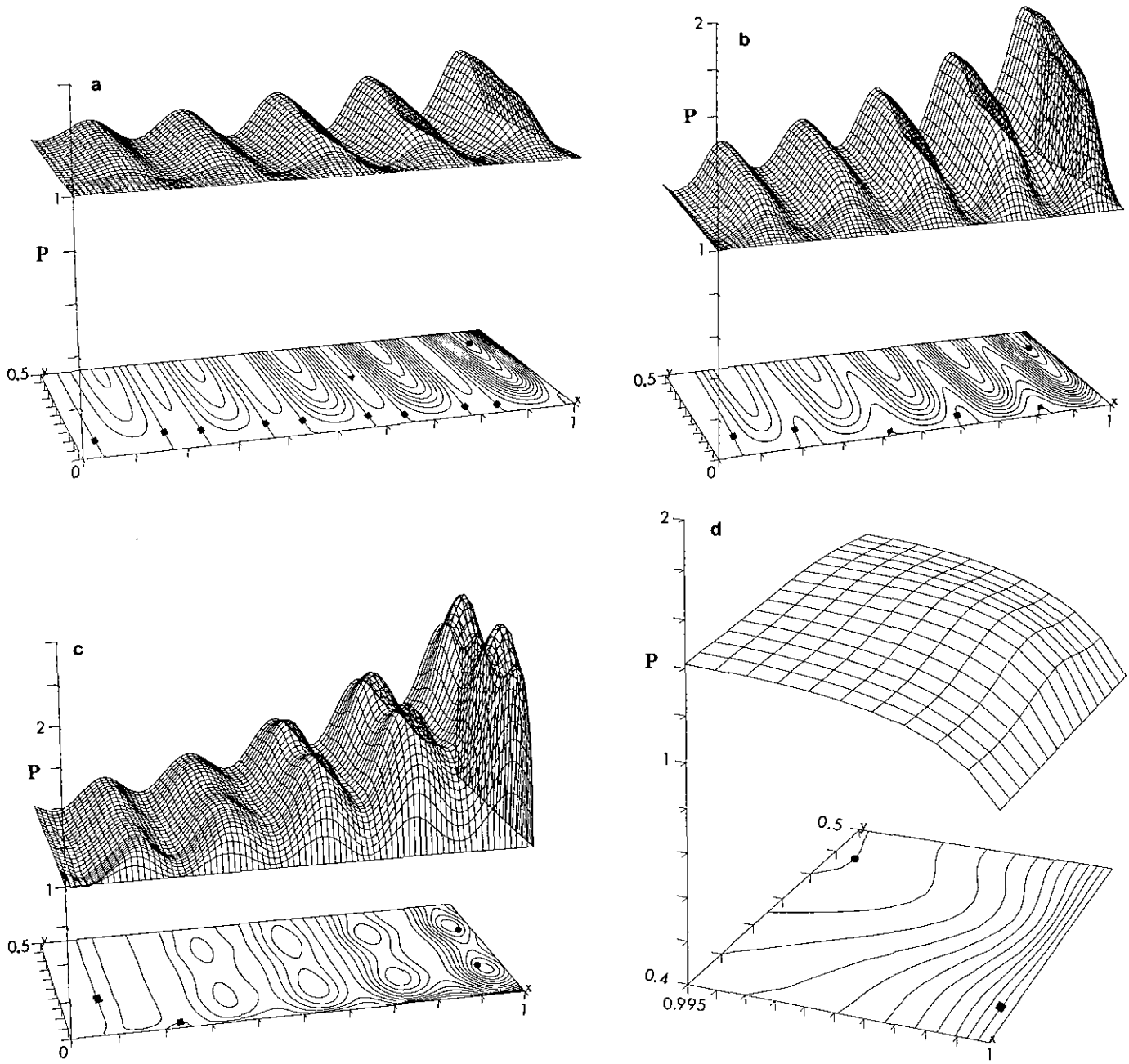

FIG. 8. (a) Pressure profile for a slider with $NWX = 5$, $NWY = 4$, and $\varepsilon_x = \varepsilon_y = 0.15$: $\Lambda = 10^2$ ($P_{\min} = 0.96$, $P_{\max} = 1.26$, $\Delta P = 0.02$). (b) Pressure profile for a slider with $NWX = 5$, $NWY = 4$, and $\varepsilon_x = \varepsilon_y = 0.15$: $\Lambda = 10^3$ ($P_{\min} = 1$, $P_{\max} = 1.75$, $\Delta P = 0.05$). (c) Pressure profile for a slider with $NWX = 5$, $NWY = 4$, and $\varepsilon_x = \varepsilon_y = 0.15$: $\Lambda = 10^5$ ($P_{\min} = 1$, $P_{\max} = 2.3$, $\Delta P = 0.1$). (d) Enlarged view of trailing edge boundary layer region in Fig. 8b ($P_{\min} = 1$, $P_{\max} = 1.55$, $\Delta P = 0.05$).

$P(x, y)$ is proportional to $1/h(x, y)$ as $\Lambda \to \infty$, which supports the observed pattern in Fig. 8c, where two humps in the y-direction and five in the x-direction can be clearly identified. The influence of the clearance height on the pressure, stemming from the non-linear gradients on the left-hand side of the Reynolds equation (2.1), is present in all three solutions but is most evident in Fig. 8c. The presence of any roughness on the stationary surface increases the load-carrying capacity (Fig. 5) of the wedge bearing, even at high values of the aspect ratio where more of the flow rate leaks through the side and does not contribute to load generation. However, these results are qualitatively similar for other choices of aspect ratio and wave amplitude. Furthermore, since roughness effects are

local in nature the conclusions of the numerical experiments should be applicable to other bearing geometries besides the specific wedge bearing considered in this study.

5. CONCLUSIONS

A four-subdomain, Chebyshev spectral collocation method for the solution of the Reynolds equation of lubrication was presented. A careful choice of the number of collocation points, where the interface conditions were applied, ensured pointwise continuity of the pressure across all subdomain interfaces. Further, collocation points were chosen on the boundaries such that the Dirichlet and Neumann conditions were satisfied identically on their corresponding segments. Relatively fewer degrees of freedom per wave were required to accurately resolve the wavy nature of the pressure solution. The domain decomposition strategy used made it possible to independently vary the number of degrees of freedom in the side and trailing edge boundary layer regions in order to accurately capture the sharp pressure gradients therein. A multiparameter continuation scheme was utilized, allowing the independent control of the progress of the solution from one bearing number or wave amplitude level to the next, all the while reducing the amount of computational effort required. The apparent success in handling the highly non-linear nature of the Reynolds equation suggests that the present method is well suited for the solution of ultra-thin gas bearing problems. The use of different sets of basis functions is presently being investigated for the class of problems where surface waviness is replaced by higher frequency texture.

ACKNOWLEDGMENTS

The first author acknowledges NSF support under Grant MSME-8810574 to study surface roughness effects on ultra-thin air bearings. The first author also acknowledges the use of the CRAY Y-MP8/864 system at the NSF San Diego Supercomputer Center located at the University of California at San Diego, as well as the use of NASA Ames' PLOT3D graphics package.

REFERENCES

1. B. Bhushan, *Tribology and Mechanics of Magnetic Storage Devices* (Springer-Verlag, New York, 1990).
2. J. P. Boyd, *Chebyshev and Fourier Spectral Methods* (Springer-Verlag, Berlin, 1989).
3. C. Canuto, M. Y. Hussaini, A. Quarteroni, and T. A. Zang, *Spectral Methods in Fluid Dynamics* (Springer-Verlag, New York, 1991).
4. L. Fox and I. Parker, *Chebyshev Polynomials in Numerical Analysis* (Oxford Univ. Press, London, 1968).
5. A. Karageorghis, Southern Methodist University, Department of Mathematics, Report No. 91-2, 1991.
6. Y. Mitsuya, *Bull. JSME* **22**, 863 (1979).
7. NAG Library Mark 13, NAG Ltd., Jordan Hill Road, Oxford, UK, 1989.
8. M. J. D. Powell, in *Numerical Methods for Nonlinear Algebraic Equations*, edited by P. Rabinowitz (Gordon & Breach, London, 1970).
9. P. E. Raad and I. M. Kuria, *ASME J. Tribol.* **111**, 719 (1989).
10. P. E. Raad and J. W. White, *ASME J. Tribol.* **111**, 41 (1989).
11. J. A. Schmitt and R. C. Diprima, *ASME J. Lubr. Technol.* **100**, 254 (1978).
12. R. Seydel, *From Equilibrium to Chaos: Practical Bifurcation and Stability Analysis*, (Elsevier, New York, 1988).
13. A. N. Varghese and P. E. Raad, Southern Methodist University, Department of Mechanical Engineering, Report No. ME-TFS-91-02, NSF grant no. MSME-8810574, 1991.
14. J. W. White and A. Nigam, *ASME J. Lubr. Technol.* **102**, 80 (1980).
15. J. W. White and P. E. Raad, *ASME J. Tribol.* **109**, 271 (1987).
16. J. W. White, P. E. Raad, A. H. Tabrizi, S. P. Ketkar, P. P. Prabhu, *ASME J. Tribol.* **108**, 171 (1986).